Nanoscale Advances

ROYAL SOCIETY OF CHEMISTRY

PAPER

View Article Online
View Journal | View Issue

Check for updates

Cite this: *Nanoscale Adv.*, 2020, **2**, 1878

Simultaneously formed and embedding-type ternary $MoSe_2/MoO_2$/nitrogen-doped carbon for fast and stable Na-ion storage†

Yuanxing Yun,[a] Jie Shao, *[ac] Xuefang Shang,[b] Wei Wang,[ad] Weibo Huang,[a] Qunting Qu *[ad] and Honghe Zheng *[ad]

Received 31st December 2019
Accepted 24th February 2020

DOI: 10.1039/c9na00815b

rsc.li/nanoscale-advances

To obtain an electrode material that is capable of manifesting high Na-ion storage capacity during long-term cycling at a rapid discharge/charge rate, ternary heterophases $MoSe_2/MoO_2$/carbon are rationally designed and synthesized through a supermolecule-assisted strategy. Through using supermolecules that are constructed from MoO_4^{2-} and polydopamine as the precursor and sulfonated polystyrene microspheres as the sacrificial template, the *in situ* formed ternary phases $MoSe_2/MoO_2$/carbon are fabricated into a hollow microspherical structure, which is assembled from ultrathin nanosheets with $MoSe_2$ and MoO_2 nanocrystallites strongly embedded in a nitrogen-doped carbon matrix. In the ternary phases, the $MoSe_2$ phase contributes to a high Na-ion storage capacity by virtue of its layered crystalline structure with a wide interlayer space, while the surrounding MoO_2 and porous nitrogen-doped carbon phases are conducive to rate behaviour and cycling stability of the ternary hybrids since both the two phases are beneficial for electronic transport and structural stability of $MoSe_2$ during repeated sodiation/desodiation reaction. The as-prepared $MoSe_2/MoO_2$/carbon manifests excellent rate behaviour (a Na-ion storage capacity of 461 mA h g^{-1} at an extremely high current density of 70 A g^{-1}) and outstanding cycle performance (610 mA h g^{-1} after 1000 cycles).

Introduction

Sodium-ion batteries (SIBs) have attracted more and more attention during the past decade due to the abundant reserves and low price of sodium-related sources. Despite the analogous electrochemical reaction process to that in lithium-ion batteries, SIBs suffer seriously from a poor rate behavior because of the sluggish sodiation/desodiation kinetics restricted by the large radius of Na^+ and low intrinsic ionic/electronic conductivity of most anode materials.[1–6] How can one obtain a SIB anode that can deliver a decent capacity at a rapid discharge/charge rate? The primary strategy is to design an anode material that could transport both Na-ions and electrons quickly. In terms of the former, it is desirable that the crystal lattice structure of active materials should provide convenient channels to facilitate the migration of Na-ions. In this regard, $MoSe_2$, as a transition metal dichalcogenide with a typical 2D graphene-like layered structure and a large interlayer distance of ≈0.65 nm, stands out from various candidates for Na-ion storage.[7–14] Based on an electrochemical conversion reaction from $MoSe_2$ to $NaSe_2$ and Mo, the theoretical capacity of $MoSe_2$ reaches 422 mA h g^{-1}, which is quite high as compared with those of other SIB anode materials.[15–18] In spite of the superior Na-ion transport ability of $MoSe_2$, its electronic conductivity is not good enough, thereby restricting its high rate behavior. So combining $MoSe_2$ with various electronically conductive carbons has been proposed and demonstrated to be an effective strategy.[19–22] $MoSe_2$-covered N, P-doped carbon nanosheets manifest an improved charge transfer kinetics and retain a capacity of 216 mA h g^{-1} at a high current density of 15 A g^{-1}.[9] Hollow carbon nanosphere encapsulated $MoSe_2$ nanosheets exhibit good rate behavior maintaining a capacity of 382 mA h g^{-1} at a current density of 10 A g^{-1}.[23] However, from the viewpoint of the structure–activity relationship, $MoSe_2$-covered carbon nanosheets cannot provide fast electron transport pathways from the top, while the hollow carbon nanosphere encapsulated $MoSe_2$ cannot ensure fast electron transport in the interior. Therefore, constructing an embedding-type structured $MoSe_2$/carbon hybrid with ultrafine $MoSe_2$ homogeneously distributed in a carbon matrix, which may offer a continuous charge transport pathway throughout

[a]College of Energy, Soochow Institute for Energy and Materials InnovationS, Soochow University, Suzhou, Jiangsu 215006, China. E-mail: qtqu@suda.edu.cn; hhzheng@suda.edu.cn; shaojie@suda.edu.cn

[b]Key Laboratory of Medical Molecular Probes, School of Basic Medical Sciences, Xinxiang Medical University, Jinsui Road 601, Xinxiang, Henan 453003, China

[c]College of Chemistry, Chemical Engineering and Material Science, Soochow University, Suzhou, Jiangsu 215006, China

[d]Suzhou Huaying New Energy Materials and Technology Co., Ltd., Suzhou, Jiangsu 215100, China

† Electronic supplementary information (ESI) available: Experimental section, Fig. S1–S15 and Tables S1 and S2. See DOI: 10.1039/c9na00815b

the whole material, seems more effective in improving the rate behavior of $MoSe_2$-based materials.

Besides the rate behavior, $MoSe_2$ is confronted with the issue of poor cycling stability when being used as the anode material of SIBs.[8] On the one hand, $MoSe_2$ as a typical two-dimensional material is most commonly fabricated into a nanosheet-like structure, which tends to restack or aggregate during repeated sodiation/desodiation, leading to gradual loss of active sites.[24] On the other hand, the as-formed Na_2Se after the first sodiation process could not be completely recovered to the $MoSe_2$ phase and might be converted to Se element in the subsequent desodiation reaction.[9,25–27] Thus the electrochemical mechanism of $MoSe_2$ after the first cycle would be analogous to those of sulfur or selenium-based cathodes in Li–S, Li–Se or Na–Se batteries involving the conversion reactions of S to Li_2S, Se to Li_2Se, or Se to Na_2Se, respectively. For these batteries, the formation of soluble polyselenide/polysulfide intermediates always leads to a severe shuttle effect and rapid capacity degradation during discharge/charge.[28,29] Various porous carbons and transition metal oxides have been adopted for physical or chemical confinement to prevent polyselenide/polysulfide dissolution from sulfur or selenium-based cathodes and improve the cycling performance of these batteries.[30–33] By analogy to these sulfur or selenium-based cathodes, the combination of $MoSe_2$ with carbons or transition metal oxides is also expected to bring about improved cycling stability of $MoSe_2$ for Na-ion storage.

With these backgrounds, this work proposes a supermolecule-assisted strategy to synthesize embedding-type structured ternary heterophases $MoSe_2/MoO_2$/carbon. Through the incomplete selenization of Mo-based oxides during pyrolysis of MoO_4^{2-}-polydopamine (Mo-PDA) supermolecules, the ternary heterophases with $MoSe_2$ and MoO_2 nanoparticles uniformly embedded in a carbon matrix are obtained. Compared to the totally selenized binary phases $MoSe_2$/carbon and unselenized binary phases MoO_2/carbon, the ternary phases $MoSe_2/MoO_2$/carbon exhibit significantly improved Na-ion storage performance. By virtue of the superior Na-ion storage capability of $MoSe_2$, good electronic conductivity of MoO_2 and carbon, and the unique embedding-type structure in which the surrounding MoO_2 and carbon phases can preserve the structural stability of $MoSe_2$, the ternary heterophases exhibit excellent rate behavior (a Na-ion storage capacity of 461 mA h g^{-1} at an extremely high current density of 70 A g^{-1}) and outstanding long-term cycling performance, maintaining a capacity of 610 mA h g^{-1} after 1000 cycles.

Experimental

Materials preparation

Sulfonated polystyrene (SPS) microspheres were prepared according to previous reports[34,35] and adopted as the sacrificial template to synthesize hollow microspherical $MoSe_2/MoO_2$/carbon. Firstly, 30 mg of SPS microspheres were dispersed in a solution mixture containing 15 mg of ammonium molybdate and 15 mg of dopamine hydrochloride dissolved in a mixed solvent of ethanol and distilled water (2/1 volume ratio). The pH of the solution is adjusted to 9 using ammonium hydroxide. The solution mixture gradually turned dark red after several hours of stirring due to the formation of MoO_4^{2-}-polydopamine (Mo-PDA) supermolecules on SPS. The SPS@Mo-PDA solid was collected from the solution through centrifugation, and then washed successively with distilled water and ethanol, and at last dried at 60 °C overnight. To prepare hollow microspherical $MoSe_2/MoO_2$/carbon ternary phases, the obtained core–shell SPS@Mo-PDA was pyrolyzed and selenized in a tube furnace with a flow of high-quality Ar gas. Se powder was used as the Se source. SPS@Mo-PDA and Se powder were separately placed at both ends of the same ceramic boat, in which Se powder was located at the upstream. The ceramic boat is kept open with no covering on it. The mass of Se powder was around three times that of SPS@Mo-PDA, and the temperature of the tube furnace was raised to 500 °C with a rate of 2 °C min^{-1} and maintained at this temperature for 3 h. Totally selenized $MoSe_2$/carbon binary phases were prepared through a similar procedure except that the heating rate was set at 1 °C min^{-1} and the temperature was maintained at 500 °C for 4 h. In addition, another empty ceramic boat was covered in an inverted position on the ceramic boat containing SPS@Mo–PDA and Se powder to ensure complete selenization. The preparation procedure of unselenized MoO_2/carbon binary phases was similar to that of $MoSe_2/MoO_2$/carbon except that Se powder was absent.

Electrochemical testing

The working electrode laminate was prepared by spreading the electrode slurry onto copper foil using a coating machine. The slurry was obtained by ultrasonically dispersing a mixture of active materials ($MoSe_2/MoO_2$/NC, MoO_2/NC or $MoSe_2$/NC), conductive agent (super-P Li), and binder (sodium alginate) in distilled water. The mass ratio of active material, conductive agent, and binder in the mixture is 7/2/1. The working electrode laminate was cut into small disks with a diameter of 13 mm using a punching machine. The average loading of active substances on each electrode disk is 1.0 mg cm^{-2}. CR-2032 type coin cells were assembled in a glovebox filled with high-purity argon using a sodium disk as the counter electrode, 1.0 M $NaClO_4$ dissolved in propylene carbonate as the electrolyte, and a glass fiber filter (Whatman) as the separator. The coin cells were galvanostatically discharged and charged at various current densities in the potential range of 0.01–3.0 V using a LAND CT2001A charge/discharge tester. The specific capacity was calculated based on the total mass of the ternary or binary composites, namely, the mass of NC was also taken into account. The cyclic voltammetric (CV) data were collected at a scan rate of 0.1 mV s^{-1} using a CHI 660C electrochemical workstation.

Results and discussion

Supermolecules that are composed of inorganic nodes/clusters uniformly dispersed in organic ligands at the molecular level can be used as the precursors to synthesize some hybrids of metal oxides and carbon. Because of the unique structure of supermolecules, the obtained metal oxide nanoparticles could be homogeneously and strongly embedded in or wrapped by the organic ligand-derived carbon matrix, which is favorable for the electronic transport throughout the whole electrode. In this work, a kind of supermolecule, MoO_4^{2-}-polydopamine complex

(denoted as Mo-PDA), is used as the precursor to synthesize ternary heterophases $MoSe_2/MoO_2$/carbon. To obtain a hierarchical hollow microspherical structure, sulfonated polystyrene (SPS) microspheres are adopted as the sacrificial template.[34,35] A schematic is shown in Fig. 1 to illustrate the formation of $MoSe_2/MoO_2$/carbon. First, SPS microspheres are dispersed in a solution mixture containing ammonium molybdate and dopamine hydrochloride, and the pH of the solution is adjusted to 9 using ammonium hydroxide. The self-polymerization of dopamine preferentially occurs on the surface of SPS microspheres due to the sulfonated and active surface of SPS. Meanwhile, the catechol groups of dopamine possess a strong complexing ability towards MoO_4^{2-} during its self-polymerization,[36–38] and thus Mo-PDA supermolecules are formed on SPS. The obtained core–shell SPS@Mo-PDA is then pyrolyzed and selenized in a tube furnace with a flow of high-quality Ar gas. During pyrolysis, the inner SPS core could decompose completely and meanwhile the Mo-PDA shell could be *in situ* converted into $MoSe_2/MoO_2$ and N-doped carbon (NC), forming a hollow microspherical structure with $MoSe_2/MoO_2$ nanoparticles uniformly embedded in the NC matrix. The N-doping of carbon originates from the fact that PDA is a N-containing precursor. The incomplete selenization of the Mo-PDA derived Mo oxides generates the ternary heterophases $MoSe_2/MoO_2$/NC. Through slightly changing the reaction parameters, totally selenized binary phases $MoSe_2$/NC can be obtained (Fig. S1†). Unselenized binary phases MoO_2/NC (Fig. S2†) are prepared through the same procedure but in the absence of Se powder.

Scanning electron microscopy (SEM) images of the intermediate SPS@Mo–PDA and end product $MoSe_2/MoO_2$/NC are shown in Fig. 2. The morphology of SPS@Mo-PDA (Fig. 2a) exhibits the same microspherical structure to that of the original SPS template. Compared to the smooth surface of pure SPS (Fig. S3†), nanosheet-like Mo-PDA is obviously grown on the surface of microspheres. After pyrolysis and selenization, the microspherical morphology is perfectly maintained, and the 2D nanosheet-like structure becomes more distinct due to the formation of crystalline-state $MoSe_2/MoO_2$/NC (Fig. 2b–d). The $MoSe_2/MoO_2$/NC microspheres possess a homogeneous diameter of around 600 nm. No extra particles or uneven aggregates are observed, suggesting that Mo-PDA supermolecules preferentially grow on the surface of SPS, which guarantees the homogeneous microspherical morphology of the product. In addition, a hollow interior is supposed to be formed in these microspheres since some holes as indicated by the red arrows in Fig. 2d are distinguishable.

The hollow interior of $MoSe_2/MoO_2$/NC microspheres is also clearly observed through transmission electron microscopy

Fig. 1 Schematic illustration of the synthesis procedure of hollow microspherical $MoSe_2/MoO_2$/carbon ternary phases.

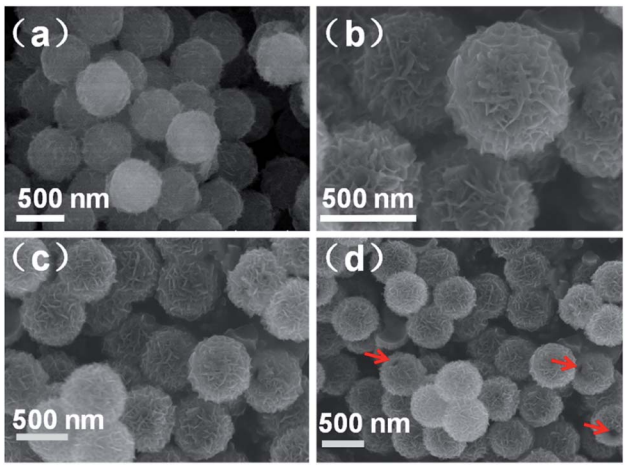

Fig. 2 SEM images of (a) the intermediate SPS@Mo-PDA and (b–d) end product $MoSe_2/MoO_2$/NC.

(TEM). As shown in Fig. 3a, the black edges are in sharp contrast to the grey central areas, and the walls of the hollow microspheres are composed of ultrathin nanosheets. From the high-resolution TEM images (Fig. 3b and S4†), the lattice fringes with interplanar spacings of 0.28 and 0.65 nm are easily found, which can be indexed to the (100) and (002) crystalline planes of $MoSe_2$, respectively. The lattice fringes with an interplanar spacing of 0.20 nm correspond to the (200) crystalline planes of MoO_2. Besides $MoSe_2$ and MoO_2 crystallites, some porous and undefined regions, which should be amorphous carbon, are distributed in the hybrid. The dimensions of $MoSe_2$ and MoO_2 crystallites are observed to be less than 5 nm, so the structure of the ternary hybrid is described as ultrasmall $MoSe_2$ and MoO_2 crystallites embedded in a carbon matrix, which is the typical structure of supermolecule-derived materials. During the preparation of the ternary $MoSe_2/MoO_2$/NC hybrid, the PDA-

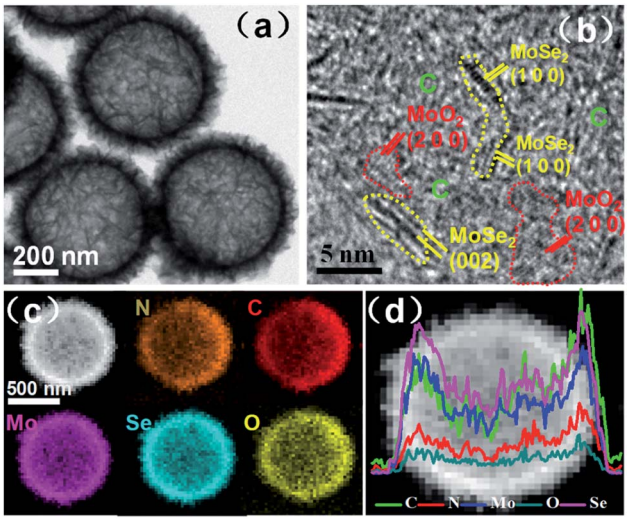

Fig. 3 (a) TEM and (b) high-resolution TEM images, (c) EDS elemental mapping images and (d) EDS linear scan profiles of hollow microspherical $MoSe_2/MoO_2$/NC ternary phases.

derived carbon plays the role of restricting the growth of $MoSe_2$ and MoO_2, thereby giving rise to the formation of ultrasmall $MoSe_2$ and MoO_2 crystallites. Moreover, the *in situ* formation of N-doped carbon and $MoSe_2/MoO_2$ through the use of the Mo-PDA precursor could generate a strong interfacial interaction among the neighbouring phases, which is beneficial for Li-ion and electron transfer across the interface.

The elemental mapping images (Fig. 3c) of the hybrid obtained through energy dispersive X-ray spectroscopy (EDS) confirm the coexistence of Mo, Se, O, C, and N elements, which are homogeneously distributed in the wall of hollow microspheres. The linear scan profiles of all the elements along the diameter of one typical microsphere (Fig. 3d) exhibit double peaks on both sides with the lowest intensity in central areas, which further demonstrate the hollow microspherical structure of the ternary hybrid. The Brunauer–Emmett–Teller (BET) surface area of $MoSe_2/MoO_2/NC$ determined by N_2 adsorption/desorption isotherms (Fig. S5†) is 190 $m^2\ g^{-1}$. Such a high surface area should originate from the porous carbon and hollow microspherical structure of the hybrid phase as observed from TEM images.

The crystalline phases of the product were further investigated using X-ray diffraction (XRD). As shown in Fig. 4a, the diffraction peaks can be well indexed to the hybrid phases of hexagonal 2H-$MoSe_2$ (JCPDS no. 29-0914) and monoclinic MoO_2 (JPCDS no. 32-0671).[39,40] Besides the typical peaks characteristic of $MoSe_2$, several weak diffraction peaks at 26.0°, 36.8° and 53.5° are well consistent with standard peaks of MoO_2, further validating the presence of MoO_2 in the composite. Notably, all the XRD peaks of $MoSe_2/MoO_2/NC$ are quite weak or broad, which is ascribed to the ultrasmall size of $MoSe_2$ and MoO_2 nanocrystallites. There are no obvious peaks characteristic of graphitic carbon, suggesting that the carbon derived from the organic ligands of Mo-PDA is mainly amorphous. Raman spectroscopy was used to further ascertain the presence of carbon and also verify the hybrid crystalline phases of $MoSe_2/MoO_2/NC$. As shown in Fig. 4b, the two characteristic peaks of carbon, D-band and G-band, appear at 1353 and 1580 cm^{-1}, respectively. Besides, the two peaks at around 237 and 287 cm^{-1} correspond to the out-of-plane A_{1g} and in-plane E^1_{2g} modes of $MoSe_2$,[41] while other peaks at 492, 573 and 745 cm^{-1} are characteristic of MoO_2.[42]

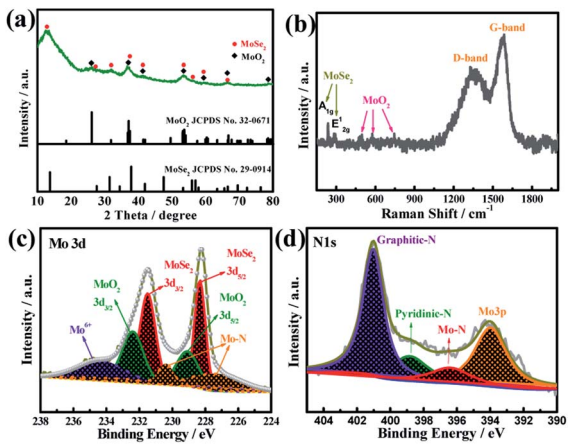

Fig. 4 (a) XRD patterns and (b) Raman spectra of $MoSe_2/MoO_2/NC$, and (c and d) the deconvoluted XPS spectra in the core-level regions of Mo 3d and N 1s.

X-ray photoelectron spectroscopy (XPS) was used to investigate the surface electronic state of each of the elements in the ternary phases $MoSe_2/MoO_2$/carbon. The survey spectrum reveals the existence of Mo, Se, O, C, and N elements (Fig. S6†). The deconvoluted spectra of the Mo 3d core level are shown in Fig. 4c. The doublet peaks at the binding energies of 231.5 and 228.3 eV can be attributed to the Mo $3d_{3/2}$ and Mo $3d_{5/2}$ spin-orbits of Mo^{4+} in the environment of $MoSe_2$, while the neighboring doublet peaks at slightly higher binding energies of 232.4 eV and 229.2 eV signify the presence of MoO_2.[13,42,43] The one broad peak at a binding energy of around 234 eV usually originates from the slight oxidation of Mo^{4+} to Mo^{6+} when the sample is exposed to air.[13] The deconvoluted satellite peaks at lower binding energies of 230.4 and 227.5 eV can be indexed to the Mo–N bond, the formation of which results from the incorporation of nitrogen into the hybrids through the use of a N-containing supermolecule precursor. The XPS spectrum of the Se 3d core level is split into two peaks at 54.9 and 53.8 eV, corresponding well with the Se $3d_{3/2}$ and Se $3d_{5/2}$ spin-orbits of Se^{2-} (Fig. S7†).[42] The deconvoluted XPS spectra of the C 1s core level (Fig. S8†) exhibit one dominant peak at 284.6 eV, which is characteristic of carbon materials. The deconvoluted XPS spectra in the core level region of N 1s are shown in Fig. 4d. The two binding energies at 398.8 and 401.1 eV can be identified as pyridinic-N and graphitic-N species located at the six-member ring of the carbon lattice. One additional peak at 396.5 eV can be attributed to the Mo–N bond.

To gain insight into the differences between the electronic states of Mo element in $MoSe_2/MoO_2/NC$, $MoSe_2/NC$, and MoO_2/NC, XPS spectra of binary MoO_2/NC and $MoSe_2/NC$ in the core-level region of Mo 3d were also measured and are shown in Fig. S9 and S10,† respectively. In the case of binary MoO_2/NC, the binding energies of 230.0 and 232.9 eV can be assigned to Mo^{4+} species, while the binding energies of 231.8 and 235.0 eV signify the presence of Mo^{6+}. The relatively high content of Mo^{6+} in the surface of MoO_2/NC could be caused by its oxidation in air since monoclinic MoO_2 is a metastable phase. Besides, one extra weak peak of Mo 3d located at 228.9 eV is correlated with the Mo–N bond. In the case of binary $MoSe_2/NC$, the doublet peaks at the binding energies of 229.2 and 232.3 eV can be attributed to the Mo $3d_{5/2}$ and Mo $3d_{3/2}$ spin-orbits of Mo^{4+} in the environment of $MoSe_2$. The oxidation of Mo^{4+} by air is not obvious for $MoSe_2/NC$ because there are no obvious peaks at higher binding energy. Moreover, there are no deconvoluted peaks characteristic of the Mo–N bond. Therefore, it is speculated that the presence of Mo^{6+} in the ternary $MoSe_2/MoO_2/NC$ should originate from the oxidation of the MoO_2 phase by air, while the Mo–N bond is most probably formed between MoO_2 and nitrogen-doped carbon phases.

All the TEM, EDS, XRD, Raman, and XPS results demonstrate that the obtained ternary hybrid $MoSe_2/MoO_2/NC$ is composed of $MoSe_2$, MoO_2, and nitrogen-doped carbon. To quantitatively analyze the content of each phase in the ternary hybrid $MoSe_2/MoO_2/NC$, elemental analysis and inductively coupled plasma

optical emission spectroscopy were used. The mass percentages of all the elements are listed in Table S1.† Through calculation, the mass fraction of $MoSe_2$, MoO_2, and nitrogen-doped carbon in the hybrid is around 39.4, 26.2, and 34.4 wt%, respectively.

The Na-ion storage performance of the as-prepared ternary phases $MoSe_2/MoO_2$/NC was investigated using a sodium disk as the counter electrode and compared with that of binary phases $MoSe_2$/NC and MoO_2/NC. Cyclic voltammetry (CV) was employed to study the redox reaction behaviour of the electrode materials and the CV curves obtained at a scan rate of 0.1 mV s^{-1} are shown in Fig. 5a, S11 and S12.† In the case of ternary phases $MoSe_2/MoO_2$/NC, during the first negative scan, there are three reduction peaks at around 1.1, 0.6, and 0.2 V, which are similar to those of $MoSe_2$-based electrodes reported in the literature.[9,21,25,27] The first reduction peak at 1.1 V is usually considered to be the intercalation of Na-ions into the $MoSe_2$ lattice accompanied by the formation of the Na_xMoSe_2 phase. The other two reduction peaks at 0.6 and 0.2 V correspond to the solid-state interphase (SEI) film formation *via* the reductive decomposition of electrolyte and the conversion reaction from Na_xMoSe_2 to Mo/Na_2Se, respectively.[44] The following positive scan corresponds to the desodiation process, during which the main oxidation peak at 1.8 V and the shoulder-like peak at 2.2 V are in good agreement with the reported oxidation peaks of $MoSe_2$-based electrodes in SIBs.[21,25] The reaction mechanisms of these oxidation peaks are still controversial. Some researchers claimed that the desodiation process should be accompanied by the reversible conversion from metallic Mo back to $MoSe_2$.[17,23,24] Also, there are some reports proposing that the desodiation process is related to the oxidation of Na_2Se rather than metallic Mo since Se instead of $MoSe_2$ is obviously formed after the desodiation process.[9,25,26] Through systematically studying the *ex situ* Raman spectra of $MoSe_2$-based electrodes at different charge/discharge potentials, Yang *et al.*[9] directly prove that Se is formed at the end of the first charge. Therefore, it is proposed that the Na-ion storage mechanism of $MoSe_2$ after the first cycle most probably involves the reversible conversion reaction from Se to Na_2Se.

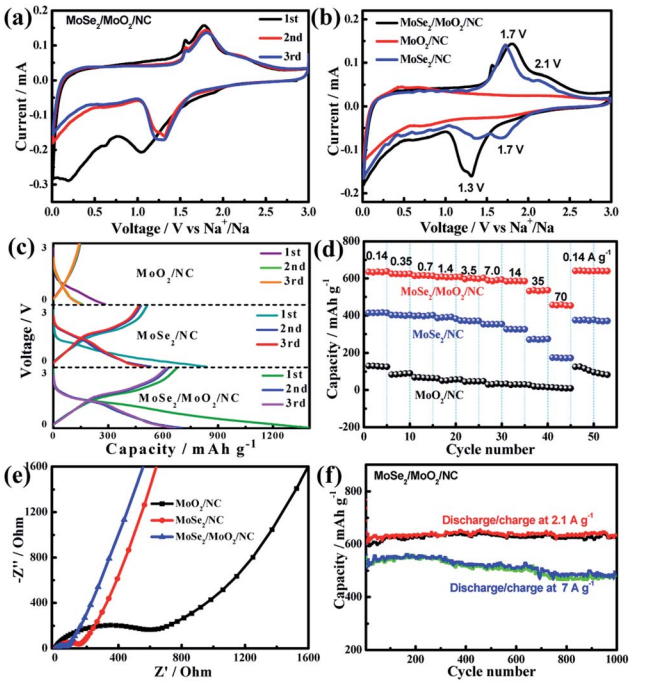

Fig. 5 (a) CV curves of $MoSe_2/MoO_2$/NC during the first three scans at a scan rate of 0.1 mV s^{-1}, (b) the CV curve comparison of $MoSe_2/MoO_2$/NC, $MoSe_2$/NC, and MoO_2/NC electrodes in the second scan, (c) the first three discharge/charge curves at a current density of 0.14 A g^{-1}, (d) the capacity evolution at various charge current rates ranging from 0.14 to 70 A g^{-1}, (e) Nyquist plots of the three hybrid electrodes after five discharge/charge cycles, and (f) long-term cycling performance of the $MoSe_2/MoO_2$/NC electrode.

The CV curves of $MoSe_2/MoO_2$/NC, $MoSe_2$/NC, and MoO_2/NC electrodes in the second cycle are compared in Fig. 5b. The two couples of redox peaks at 1.7/2.1 V and 1.3/1.7 V observed for binary phases $MoSe_2$/NC are typical of $MoSe_2$-based electrodes in SIBs. Abouimrane *et al.*[45] previously studied the Na-ion storage behaviour of a Se electrode and observed two discharge plateaus at 1.9 and 1.5 V in the sodiation process, so they proposed a multi-phase conversion reaction of Se, where intermediate phase polyselenides may be formed. The two reduction peaks of $MoSe_2$/NC in the second cycle appear at similar potentials of 1.7 and 1.3 V, which actually should correspond to two potential plateaus in the discharge curves, further suggesting that the Na-ion storage mechanism of $MoSe_2$ should be analogous to that of Se. So, intermediate phase polyselenides could also be formed during the cycling of $MoSe_2$-based electrodes.[42] The dissolution and shuttling of polyselenides may lead to a rapid capacity decline of $MoSe_2$-based electrodes. In the case of binary phases MoO_2/NC, no significant redox peaks are observed due to the poor Na-ion storage ability of MoO_2. Through comparing the CV curves of $MoSe_2/MoO_2$/NC and $MoSe_2$/NC, the main differences lie in that the first reduction peak of $MoSe_2$/NC at 1.7 V is not clearly defined for $MoSe_2/MoO_2$/NC, but the reduction peak intensity of $MoSe_2/MoO_2$/NC at a lower potential of 1.3 V is much stronger. So it is assumed that such *in situ* formed ternary phases $MoSe_2/MoO_2$/NC could preclude the formation of intermediate phase polyselenides, which will be beneficial for the structural stabilization of electrodes during charge/discharge cycling.

Out of interest, the Li-ion storage behaviour of $MoSe_2/MoO_2$/NC, $MoSe_2$/NC, and MoO_2/NC is also investigated through CV (Fig. S13–S15†). In terms of MoO_2/NC, the two couples of sharp redox peaks at 1.3/1.4 V and 1.6/1.7 V correspond to the phase conversion of MoO_2 upon lithiation/delithiation.[46] The CV curves of $MoSe_2$/NC exhibit one couple of reversible redox peaks at 1.8/2.2 V, which are very similar to those of Se-based electrodes in Li–Se batteries.[28,30,47] So the Li-ion storage mechanism of $MoSe_2$ after the first cycle is acknowledged to be based on the reversible conversion reaction of Se to Li_2Se.[48] By analogy to the Li-ion storage of $MoSe_2$, it is most likely that $MoSe_2$ would exhibit a similar conversion reaction of Se to Na_2Se. In the case of ternary phases $MoSe_2/MoO_2$/NC, the redox peaks of both MoO_2 and $MoSe_2$ are clearly identified, which is another piece of evidence proving the co-existence of $MoSe_2$ and MoO_2 in the hybrid.

The first three discharge/charge curves of the as-prepared hybrids at a current density of 0.14 A g^{-1} are shown in Fig. 5c.

The reversible (charge) capacity of MoO_2/NC is quite low (around 124 mA h g^{-1}), and this is because the crystalline structure of MoO_2 is not favorable for Na-ion storage. The discharge curves of $MoSe_2$/NC exhibit a sloping potential plateau at around 1.5 V, corresponding to the two reduction peaks at around 1.7 and 1.3 V in CV curves. The reversible capacity of $MoSe_2$/NC in the second cycle is around 413 mA h g^{-1}, close to the theoretical capacity of $MoSe_2$. By comparison with $MoSe_2$/NC, $MoSe_2$/MoO_2/NC manifests a similar potential change tendency during discharge/charge, while its capacity is considerably enhanced. The reversible capacity of $MoSe_2$/MoO_2/NC at a current density of 0.14 A g^{-1} in the second cycle is around 634 mA h g^{-1}, which is significantly higher than that of carbon nanosphere encapsulated $MoSe_2$ (498 mA h g^{-1} at 0.1 A g^{-1}),[25] $MoSe_2$-covered N, P-doped carbon nanosheets (454 mA h g^{-1} at 0.5 A g^{-1}),[9] and MoO_2 nanocluster decorated $MoSe_2$/graphene (422 mA h g^{-1} at 0.1 A g^{-1}).[42] To calculate the theoretical capacity of the ternary $MoSe_2$/MoO_2/NC phases, the theoretical capacity and mass fraction of each phase should be considered. The theoretical capacity of $MoSe_2$ for Na-ion storage is 422 mA h g^{-1}. However, it is difficult to determine the theoretical capacities of the other two phases MoO_2 and NC because their crystalline structures are unfavorable for Na-ion storage and their Na-ion storage capacity should mainly be capacitive. So here the practical capacity of MoO_2/NC (124 mA h g^{-1}) is assumed as the theoretical capacity of the other two components (MoO_2/NC). Taking the mass fractions of $MoSe_2$ and MoO_2/NC (39.4% and 60.6%, respectively) into consideration, the theoretical capacity of the ternary phases is calculated to be 241 mA h g^{-1}. The considerably enhanced capacity of $MoSe_2$/MoO_2/NC as compared to the theoretical value suggests a strong synergistic effect of the ternary phases for Na-ion storage.[49] Firstly, the numerous pores in $MoSe_2$/MoO_2/NC as observed from TEM images are capable of accommodating Na-ions. Especially, the PDA-derived N-doped porous carbon can provide more active sites for Na-ion storage than undoped carbon. Secondly, the unique structure of $MoSe_2$/MoO_2/NC with ultrasmall $MoSe_2$/MoO_2 nanocrystallites uniformly embedded in the carbon matrix not only increases the electroactive sites but also favours electronic transport, thereby giving rise to a high utilization efficiency of active materials. Thirdly, the polymer/gel-like film formed on the electrode surface could reversibly store/release Na-ions, which generates some extra capacity for the $MoSe_2$/MoO_2/NC electrode. Lastly, besides the Na-ions stored in the bulk phase of $MoSe_2$, some Na-ions may be stored in the pores or interstices of the ternary phases $MoSe_2$/MoO_2/NC. Pak and Stucky *et al.*[50] reported that nanoscale pore engineering of MoO_2 enables the formation of a metallic Li-rich phase between the Li-ion intercalated MoO_2 phase, so its practical Li-storage capacity is considerably higher than the theoretical value. Similarly, it is also very probable that a metallic Na-rich phase may be formed in pores or interstices during the sodiation of $MoSe_2$/MoO_2/NC. All these factors contribute to the high capacity of the ternary phases $MoSe_2$/MoO_2/NC.

The rate behaviour of the as-prepared hybrids was tested by discharging the electrodes at a current density of 0.14 A g^{-1} and charging them at various current rates ranging from 0.14 to 70 A g^{-1}. As shown in Fig. 5d, the $MoSe_2$/MoO_2/NC electrode exhibits an average capacity of 611, 594, 534, and 461 mA h g^{-1} at current densities of 1.4, 7.0, 35, and 70 A g^{-1}, respectively. Once the current density is returned to 0.14 A g^{-1}, the capacity rapidly recovers to 640 mA h g^{-1}. The maximum current density used for the rate behaviour evaluation of $MoSe_2$-based electrodes in previous reports is usually up to 10 A g^{-1}. The high capacity of $MoSe_2$/MoO_2/NC at extremely high current densities of 35 and 70 A g^{-1} suggests its excellent high-rate capability, which undoubtedly should be related to the unique structure of ternary phases. In the $MoSe_2$/MoO_2/NC hybrid, ultrasmall $MoSe_2$ and MoO_2 nanocrystallites are strongly embedded into or surrounded by carbon, which can offer omnibearing electronic transport pathways through the whole electrode. Compared to the $MoSe_2$/carbon nanocomposites with carbon coated onto or encapsulated into $MoSe_2$ active materials, where the carbon can not provide effective conductive pathways from the bottom or top, the supermolecule-derived embedding-type $MoSe_2$/MoO_2/carbon nanocomposites possess unique advantages in electron transport. The nitrogen-doping of carbon can further increase its electronic conductivity, benefit its affinity to electrolyte, and also increase its electroactive sites for Na-ion storage. Furthermore, in the ternary $MoSe_2$/MoO_2/NC nanocomposites, the presence of the Mo–N bond as revealed by the XPS results could lead to an enhanced interfacial interaction between $MoSe_2$/MoO_2 and N-doped carbon because some nitrogen may be simultaneously coordinated to Mo and C. As a result, an intimate contact between $MoSe_2$/MoO_2 and N-doped carbon is achieved, which will facilitate the transport of electrons and Na-ions across the interface of heterophases. The good electronic conductivity of MoO_2 resulting from the existence of delocalized electrons in its conduction band also facilitates the electronic transport of the ternary $MoSe_2$/MoO_2/NC electrode.[46,51–53] In addition, the porous structure of carbon and ultrasmall nanocrystallite size of $MoSe_2$/MoO_2 can facilitate the access of electrolyte to the active material and shorten the diffusion distance of Na-ions in the electrode bulk. As a result, not only the charge-transfer reactions on the electrode/electrolyte interfaces but also the diffusion of Na-ions in the solid phase will be favourable, which bring about the excellent rate behaviour of $MoSe_2$/MoO_2/NC. By contrast, the binary phases MoO_2/NC exhibit extremely low capacity at high current rates due to the low Na-ion storage capability of MoO_2. The reversible capacities of $MoSe_2$/NC at various current rates are obviously lower than those of $MoSe_2$/MoO_2/NC, suggesting the synergistic effect of ternary phases for improving the Na-ion storage capacity and rate performance.

To gain insight into the electrode reaction dynamics of $MoSe_2$/MoO_2/NC, $MoSe_2$/NC, and MoO_2/NC, electrochemical impedance spectroscopy (EIS) was used. The Nyquist plots of the three electrodes after five complete sodiation/desodiation cycles are shown in Fig. 5e. The diameters of the depressed semicircles at medium-to-high frequency reflect the charge-transfer resistance (R_{ct}) occurring on the electrode/electrolyte interface, while the inclined lines in the low frequency zone are ascribed to Warburg impedance, which is associated with solid-state Na-ion diffusion in the electrode bulk.[44] The R_{ct} value of $MoSe_2$/MoO_2/NC, $MoSe_2$/NC, and MoO_2/NC is 67, 154, and 627 Ω, respectively. As we know, the

charge-transfer reaction dynamics of the electrode is related to the transport of both electrons and Na-ions. Even though MoO_2 should have better electronic conductivity, its Na-ion transport ability should be very poor during the electrochemical reactions as reflected by its very low Na-ion storage capacity. The much lower R_{ct} of $MoSe_2$/NC as compared to that of MoO_2/NC suggests that the Na-ion transport ability of the electrode is also of great importance for a decreased R_{ct}. Therefore, a synergistic effect of $MoSe_2$ and MoO_2 gives rise to the lowest R_{ct} of ternary $MoSe_2/MoO_2$/NC, suggesting a rapid charge transfer reaction on the electrode/electrolyte interface. As estimated from the slope of the inclined lines at low frequency, the Na-ion diffusion resistance in the MoO_2/NC electrode should be significantly higher than that in the other two electrodes. The different rate behaviour of $MoSe_2/MoO_2$/NC, $MoSe_2$/NC, and MoO_2/NC can be perfectly explained by their different charge transfer and Na-ion diffusion resistances. Specifically, the lower the resistances are, the better the rate behaviour is.

The long-term cycling performance of the $MoSe_2/MoO_2$/NC electrode is shown in Fig. 5f. The reversible capacity of $MoSe_2/MoO_2$/NC discharged/charged at 2.1 A g^{-1} is stabilized at around 610 mA h g^{-1} after the initial several formation cycles, and manifests negligible degradation during the subsequent 1000 cycles. At a higher discharge/charge rate of 7 A g^{-1}, the reversible capacity of the 1000th cycle is around 480 mA h g^{-1}, equalling to a capacity retention of around 91%. The electrochemical performance of some previously reported $MoSe_2$-based anodes for Na-ion batteries is summarized in Table S2.† For instance, $MoSe_2$-covered N, P-doped carbon nanosheets exhibit an initial Na-ion storage capacity of 378 mA h g^{-1} and a capacity retention of 87% after 1000 cycles at 0.5 A g^{-1};[9] encapsulation-type structured $MoSe_2$@hollow carbon nanospheres preserve a capacity of 501 mA h g^{-1} after 1000 cycles at 1 A g^{-1}.[23] These comparative data suggest the outstanding cycling stability of $MoSe_2/MoO_2$/NC for Na-ion storage, which undoubtedly is related to its unique structure and ternary phase composition. The pores and voids in the hierarchical structured $MoSe_2/MoO_2$/NC hollow microspheres assembled from ultrathin nanosheets work as the buffering areas to alleviate the volume change of $MoSe_2$ upon sodiation/desodiation, enabling the electrode structure to be stable. TEM images of the $MoSe_2/MoO_2$/NC electrode after 1000 cycles (Fig. 6) show that not only the hollow microspherical structure but also the overall dimensions of these microspheres are well maintained, validating the structural stability of $MoSe_2/MoO_2$/NC during repeated sodiation/desodiation reaction. Also, the embedding-type structure of the *in situ* formed ternary phases $MoSe_2/MoO_2$/NC renders a good contact among the three heterophases, and the surrounding MoO_2 and NC phases can restrict the aggregation of $MoSe_2$ active materials during long-term cycling. In addition, by analogy to the sulphur-based cathodes in Li–S batteries, where both porous MoO_2 and nitrogen-doped carbon have been combined with sulphur to prevent polysulfide dissolution and improve the cycling performance,[32,42] the presence of MoO_2 and nitrogen-doped carbon in the ternary phases $MoSe_2/MoO_2$/NC is supposed to play the same role of trapping polyselenides generated by the sodiation/desodiation reaction of $MoSe_2$. Correspondingly, the cycling performance of $MoSe_2/MoO_2$/NC for Na-ion storage is significantly improved through the rational construction of embedding-type structured ternary phases.

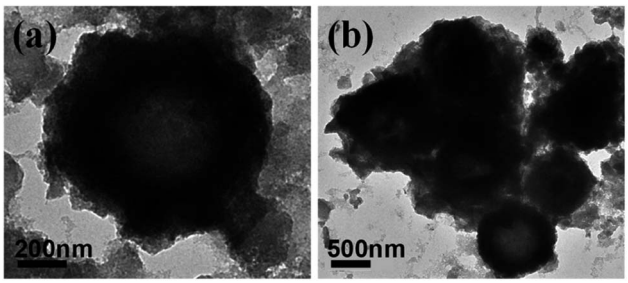

Fig. 6 TEM images of $MoSe_2/MoO_2$/NC after 1000 sodiation/desodiation cycles.

Conclusions

Strongly coupled ternary heterophases $MoSe_2/MoO_2$/NC are rationally designed and synthesized through a supermolecule-assisted strategy. The supermolecule-derived ternary phases are composed of $MoSe_2$ and MoO_2 nanocrystallites uniformly embedded in a nitrogen-doped carbon matrix. Compared to the binary phases $MoSe_2$/NC and MoO_2/NC, the ternary phases exhibit a strong synergistic effect for improving the Na-ion storage performance. The large interlayer space of $MoSe_2$ favours Na-ion transport and storage. The surrounding electronically conductive MoO_2 nanocrystallites and porous nitrogen-doped carbon not only provide fast electronic transport pathways through the whole electrode, but also play a role in preventing aggregation, alleviating volume change and trapping polyselenides engendered by the sodiation/desodiation reaction of $MoSe_2$. As a result, the ternary phases manifest excellent rate behaviour and outstanding long cycle life. Such a supermolecule-assisted protocol for the *in situ* formation of ternary heterophases would provide a new strategy for the designed synthesis of superior nanocomposite electrodes for various applications in energy storage and conversion systems.

Conflicts of interest

There are no conflicts to declare.

Acknowledgements

This work was supported by the National Natural Science Foundation of China (NSFC no. 21301124 and 21875156) and The Natural Science Foundation of the Jiangsu Higher Education Institutions of China (18KJD150004).

Notes and references

1 P. K. Nayak, L. Yang, W. Brehm and P. Adelhelm, *Angew. Chem., Int. Ed.*, 2018, **57**, 102–120.
2 H. Zhang, I. Hasa and S. Passerini, *Adv. Energy Mater.*, 2018, **8**, 1702582.

3 C. Delmas, *Adv. Energy Mater.*, 2018, **8**, 1703137.
4 H. Han, X. Chen, J. Qian, F. Zhong, X. Feng, W. Chen, X. Ai, H. Yang and Y. Cao, *Nanoscale*, 2019, **11**, 21999–22005.
5 D. Cao, W. Kang, S. Wang, Y. Wang, K. Sun, L. Yang, X. Zhou, D. Sun and Y. Cao, *J. Mater. Chem. A*, 2019, **7**, 8268–8276.
6 Y. Wang, W. Kang, D. Cao, M. Zhang, Z. Kang, Z. Xiao, R. Wang and D. Sun, *J. Mater. Chem. A*, 2018, **6**, 4776–4782.
7 A. Eftekhari, *Appl. Mater. Today*, 2017, **8**, 1–17.
8 D. Xie, X. Xia, Y. Zhong, Y. Wang, D. Wang, X. Wang and J. Tu, *Adv. Energy Mater.*, 2017, **7**, 1601804.
9 F. Niu, J. Yang, N. Wang, D. Zhang, W. Fan, J. Yang and Y. Qian, *Adv. Funct. Mater.*, 2017, **27**, 1700522.
10 J. Ge, L. Fan, J. Wang, Q. Zhang, Z. Liu, E. Zhang, Q. Liu, X. Yu and B. Lu, *Adv. Energy Mater.*, 2018, **8**, 1801477.
11 L. Zeng, B. Kang, F. Luo, Y. Fang, C. Zheng, J. Liu, R. Liu, Q. Chen, M. Wei and Q. Qian, *Chem.–Eur. J.*, 2019, **25**, 13411–13421.
12 J. Chen, A. Pan, Y. Wang, X. Cao, W. Zhang, X. Kong, Q. Su, J. Lin, G. Cao and S. Liang, *Energy Storage Mater.*, 2019, **21**, 97–106.
13 J. Zhang, M. Wu, T. Liu, W. Kang and J. Xu, *J. Mater. Chem. A*, 2017, **5**, 24859–24866.
14 J. Zhang, W. Kang, M. Jiang, Y. You, Y. Cao, T.-W. Ng, D. Y. W. Yu, C.-S. Lee and J. Xu, *Nanoscale*, 2017, **9**, 1484–1490.
15 J. Gao, Y. Li, L. Shi, J. Li and G. Zhang, *ACS Appl. Mater. Interfaces*, 2018, **10**, 20635–20642.
16 C. Zhao, H. Song, Q. Zhuang, Q. Ma, J. Liang, H. Peng, C. Mao, Z. Zhang and G. Li, *Inorg. Chem. Front.*, 2018, **5**, 1026–1032.
17 H. Wang, X. Lan, D. Jiang, Y. Zhang, H. Zhong, Z. Zhang and Y. Jiang, *J. Power Sources*, 2015, **283**, 187–194.
18 W. Kang, Y. Wang, D. Cao, Z. Kang and D. Sun, *J. Alloys Compd.*, 2018, **743**, 410–418.
19 G. D. Park, J. H. Kim, S.-K. Park and Y. C. Kang, *ACS Appl. Mater. Interfaces*, 2017, **9**, 10673–10683.
20 X. Zhao, W. Cai, Y. Yang, X. Song, Z. Neale, H.-E. Wang, J. Sui and G. Cao, *Nano Energy*, 2018, **47**, 224–234.
21 H. Liu, B. Liu, H. Guo, M. Liang, Y. Zhang, T. Borjigin, X. Yang, L. Wang and X. Sun, *Nano Energy*, 2018, **51**, 639–648.
22 Y. Wang, Y. Wang, W. Kang, D. Cao, C. Li, D. Cao, Z. Kang, D. Sun, R. Wang and Y. Cao, *Adv. Sci.*, 2019, **6**, 1801222.
23 H. Liu, H. Guo, B. Liu, M. Liang, Z. Lv, K. R. Adair and X. Sun, *Adv. Funct. Mater.*, 2018, **28**, 1707480.
24 Y. C. Tang, Z. B. Zhao, Y. W. Wang, Y. F. Dong, Y. Liu, X. Z. Wang and J. S. Qiu, *ACS Appl. Mater. Interfaces*, 2016, **8**, 32324–32332.
25 P. Ge, H. Hou, C. E. Banks, C. W. Foster, S. Li, Y. Zhang, J. He, C. Zhang and X. Ji, *Energy Storage Mater.*, 2018, **12**, 310–323.
26 D. Xie, W. Tang, Y. Wang, X. Xia, Y. Zhong, D. Zhou, D. Wang, X. Wang and J. Tu, *Nano Res.*, 2016, **9**, 1618–1629.
27 Y. N. Ko, S. H. Choi, S. B. Park and Y. C. Kang, *Nanoscale*, 2014, **6**, 10511–10515.
28 C. Luo, Y. Xu, Y. Zhu, Y. Liu, S. Zheng, Y. Liu, A. Langrock and C. Wang, *ACS Nano*, 2013, **7**, 8003–8010.
29 Y. Cui, X. Zhou, W. Guo, Y. Liu, T. Li, Y. Fu and L. Zhu, *Batteries Supercaps*, 2019, **2**, 784–791.
30 C. Luo, J. Wang, L. Suo, J. Mao, X. Fan and C. Wang, *J. Mater. Chem. A*, 2015, **3**, 555–561.
31 L. Zeng, X. Chen, R. Liu, L. Lin, C. Zheng, L. Xu, F. Luo, Q. Qian, Q. Chen and M. Wei, *J. Mater. Chem. A*, 2017, **5**, 22997–23005.
32 Q. Qu, T. Gao, H. Zheng, Y. Wang, X. Li, X. Li, J. Chen, Y. Han, J. Shao and H. Zheng, *Adv. Mater. Interfaces*, 2015, **2**, 1500048.
33 T. Gao, J. Shao, X. Li, G. Zhu, Q. Lu, Y. Han, Q. Qu and H. Zheng, *Chem. Commun.*, 2015, **51**, 12459–12462.
34 Z. Wan, J. Shao, J. Yun, H. Zheng, T. Gao, M. Shen, Q. Qu and H. Zheng, *Small*, 2014, **10**, 4975–4981.
35 X. Li, X. Zheng, J. Shao, T. Gao, Q. Shi and Q. Qu, *Chem.–Eur. J.*, 2016, **22**, 376–381.
36 C. Wang, L. Sun, F. Zhang, X. Wang, Q. Sun, Y. Cheng and L. Wang, *Small*, 2017, **13**, 1701246.
37 D. Sun, Y. Tang, D. Ye, J. Yan, H. Zhou and H. Wang, *ACS Appl. Mater. Interfaces*, 2017, **9**, 5254–5262.
38 Y. Huang, Q. Gong, X. Song, K. Feng, K. Nie, F. Zhao, Y. Wang, M. Zeng, J. Zhong and Y. Li, *ACS Nano*, 2016, **10**, 11337–11343.
39 S. Deng, Y. Zhong, Y. Zeng, Y. Wang, Z. Yao, F. Yang, S. Lin, X. Wang, X. Lu, X. Xia and J. Tu, *Adv. Mater.*, 2017, **29**, 1700748.
40 Y. Yun, J. Shao, Y. Chen, Z. Cao, Q. Qu and H. Zheng, *ACS Appl. Nano Mater.*, 2019, **2**, 1883–1889.
41 Z. Luo, J. Zhou, L. Wang, G. Fang, A. Pan and S. Liang, *J. Mater. Chem. A*, 2016, **4**, 15302–15308.
42 X. Zhao, H.-E. Wang, Y. Yang, Z. G. Neale, R. C. Massé, J. Cao, W. Cai, J. Sui and G. Cao, *Energy Storage Mater.*, 2018, **12**, 241–251.
43 X. Zhao, J. Sui, F. Li, H. Fang, H. Wang, J. Li, W. Cai and G. Cao, *Nanoscale*, 2016, **8**, 17902–17910.
44 Z.-T. Shi, W. Kang, J. Xu, L.-L. Sun, C. Wu, L. Wang, Y.-Q. Yu, D. Y. W. Yu, W. Zhang and C.-S. Lee, *Small*, 2015, **11**, 5667–5674.
45 A. Abouimrane, D. Dambournet, K. W. Chapman, P. J. Chupas, W. Weng and K. Amine, *J. Am. Chem. Soc.*, 2012, **134**, 4505–4508.
46 Y. Yun, Z. Shi, J. Shao, Q. Qu, Y. Gao, Z. Chen, Y. Chen and H. Zheng, *ChemNanoMat*, 2018, **4**, 1247–1253.
47 Y. J. Hong, K. C. Roh and Y. Chan Kang, *J. Mater. Chem. A*, 2018, **6**, 4152–4160.
48 M. Yousaf, Y. Wang, Y. Chen, Z. Wang, W. Aftab, A. Mahmood, W. Wang, S. Guo and R. P. S. Han, *ACS Appl. Mater. Interfaces*, 2018, **10**, 14622–14631.
49 Y. Shi, C. Hua, B. Li, X. Fang, C. Yao, Y. Zhang, Y.-S. Hu, Z. Wang, L. Chen, D. Zhao and G. D. Stucky, *Adv. Funct. Mater.*, 2013, **23**, 1832–1838.
50 J. K. Shon, H. S. Lee, G. O. Park, J. Yoon, E. Park, G. S. Park, S. S. Kong, M. Jin, J.-M. Choi, H. Chang, S. Doo, J. M. Kim, W.-S. Yoon, C. Pak, H. Kim and G. D. Stucky, *Nat. Commun.*, 2016, **7**, 11049.
51 B. Hu, L. Mai, W. Chen and F. Yang, *ACS Nano*, 2009, **3**, 478–482.
52 C. Jian, Q. Cai, W. Hong, J. Li and W. Liu, *Small*, 2018, **14**, 1703798.
53 X. Chen, G. Liu, W. Zheng, W. Feng, W. Cao, W. Hu and P. Hu, *Adv. Funct. Mater.*, 2016, **26**, 8537–8544.